Turbulent 2.5-dimensional dynamos

K. Seshasayanan[1],† and A. Alexakis[1]

[1]Laboratoire de Physique Statistique, École Normale Supérieure, PSL Research University;
Université Paris Diderot Sorbonne Paris-Cité; Sorbonne Universités UPMC Univ Paris 06; CNRS;
24 rue Lhomond, 75005 Paris, France

We study the linear stage of the dynamo instability of a turbulent two-dimensional flow with three components $(u(x, y, t), v(x, y, t), w(x, y, t))$ that is sometimes referred to as a 2.5-dimensional (2.5-D) flow. The flow evolves based on the two-dimensional Navier–Stokes equations in the presence of a large-scale drag force that leads to the steady state of a turbulent inverse cascade. These flows provide an approximation to very fast rotating flows often observed in nature. The low dimensionality of the system allows for the realization of a large number of numerical simulations and thus the investigation of a wide range of fluid Reynolds numbers Re, magnetic Reynolds numbers Rm and forcing length scales. This allows for the examination of dynamo properties at different limits that cannot be achieved with three-dimensional simulations. We examine dynamos for both large and small magnetic Prandtl-number turbulent flows $Pm = Rm/Re$, close to and away from the dynamo onset, as well as dynamos in the presence of scale separation. In particular, we determine the properties of the dynamo onset as a function of Re and the asymptotic behaviour in the large Rm limit. We are thus able to give a complete description of the dynamo properties of these turbulent 2.5-D flows.

Key words: dynamo theory, MHD and electrohydrodynamics, turbulent flows

1. Introduction

The dynamo instability caused by the motion of conducting fluids is the main source of magnetic-field generation in astrophysical objects such as planets, stars, the interstellar medium and galaxies. In many cases these objects are rotating, rendering the flow strongly anisotropic (Pedlosky 1987; Izakov 2013). The Coriolis force, caused by rotation, suppresses the variations along the axis of rotation, leading the flows to become to some extent two-dimensionalized and dependent on only two spacial coordinates, although in some cases retaining all three velocity components, depending on the boundary conditions. This result was first shown in Hough (1897) for linear perturbations and proven in more detail in Taylor (1917) and Proudman (1916). The tendency for rotating flows to become two-dimensionalized and the implications of this have been further examined in theoretical investigations (Hopfinger & van Heijst 1993; Waleffe 1993; Scott 2014), numerical simulations (Hossain 1994; Yeung & Zhou 1998; Smith & Waleffe 1999; Chen *et al.* 2005; Thiele & Müller 2009;

† Email address for correspondence: skannabiran@lps.ens.fr

Mininni & Pouquet 2010; Yoshimatsu, Midorikawa & Kaneda 2011; Sen *et al.* 2012; Deusebio *et al.* 2014; Alexakis 2015) and laboratory experiments (Sugihara, Migita & Honji 2005; Staplehurst, Davidson & Dalziel 2008; van Bokhoven *et al.* 2009; Yarom, Vardi & Sharon 2013; Campagne *et al.* 2014; Gallet *et al.* 2014). The extent of this two-dimensionalization depends on the rotation rate and is subject to current investigation (Nazarenko & Schekochihin 2011; Baqui & Davidson 2015). Recently, theoretical work has shown that the flow becomes exactly two-dimensional (2-D) for free-slip or periodic boundary conditions provided that the rotation is above a critical value (Gallet 2015). This allows one to consider the large-rotation limit which leads to a flow $(u(x, y, t), v(x, y, t), w(x, y, t))$ that is independent of the coordinate along the axis of rotation (from here on taken as the *z*-direction). These flows are referred to in the literature as 'two-and-a-half'-dimensional (2.5-D) flows or the $2 + \epsilon$ model.

Two-dimensionalization of the flow drastically alters its statistical properties. Perhaps the most important consequence is the change in the direction of the energy cascade: whereas three-dimensional (3-D) flows cascade energy to small scales, 2-D flows cascade energy to large scales. The small scales in 2-D turbulence are controlled by the forward cascade of the enstrophy (the second invariant of the 2-D Navier–Stokes equations). The fate of the energy that cascades to the large scales depends on the presence or absence of a dissipation mechanism at large scales. In the presence of such dissipation (as in, for example, Ekman friction (Pedlosky 1987)), the injected energy that cascades to the large scales is balanced and the Kolmogorov power-law energy spectrum $E(k) \propto k^{-5/3}$ is formed (Boffetta & Ecke 2012). In its absence, however, energy accumulates at the large scales leading to condensates that take the form of vortex dipoles (Kraichnan 1967; Chertkov *et al.* 2007; Laurie *et al.* 2014). This process leads to saturation when the dipole amplitude is so large that viscous dissipation at the large scales balances the inversely cascading energy, leading to an amplitude that is inversely proportional to viscosity. In fact, it can be shown that for single mode forcing and in the absence of any large-scale dissipation, both energy and enstrophy are dissipated by viscosity at large scales (Constantin, Foias & Manley 1994; Eyink 1996; Alexakis & Doering 2006). The energy spectra in this case are not power laws but are instead peaked at the smallest wavenumbers. Thus, in many respects these flows have a more laminar than turbulent behaviour irrespective of the value of the Reynolds number which can be very large. It is not surprising then, that these two different situations (with or without large-scale dissipation) have different dynamo properties and require separate treatment.

The importance of rotation on the dynamo properties of stellar and planetary flows has been known for some time (Proctor & Gilbert 1995; Davidson 2014). Clearly, when rotation is strong enough so that the flow is two-dimensionalized, the dynamo properties differ from 3-D isotropic flows. A strict 2-D flow (two dimensions, two components) does not give rise to dynamo instability (Zel'dovich 1958). However, 2.5-D flow can result in dynamo instability and thus it is perhaps the simplest dynamo flow to be examined that can merit analytical and low-cost numerical treatment. One of the first dynamo studies of 2.5-D flows was done by Roberts (1972); it examined four different laminar 2.5-D flows. The flows were stationary, which prevents Lagrangian trajectories from being chaotic in two dimensions. Since chaotic Lagrangian trajectories are required for fast dynamos (dynamos whose growth rate remains finite in the high-conductivity limit) (Vishik 1989), the resulting dynamos were slow (dynamos whose growth rate decays to zero in the high conductivity limit). However, time-dependent 2.5-D flows allow for the presence of chaos and thus pose a computationally tractable system to investigate the existence of fast dynamos.

Two-and-a-half dimensional flows were in fact the first smooth flows to demonstrate fast dynamo action (Galloway & Proctor 1992; Otani 1993). The low computational cost also makes it possible to examine flows with scale separation between the velocity length scale and the domain size. This allows mean field theories that predict large-scale dynamo action (alpha dynamos) in the large magnetic Reynolds number limit to be tested (see Courvoisier, Hughes & Tobias 2006; Rädler & Brandenburg 2009). Finally, 2.5-D flows were recently the first to show the propagation of large dynamo waves (Tobias & Cattaneo 2013; Cattaneo & Tobias 2014), whose existence was postulated more than 60 years ago (Parker 1955).

Dynamo studies of turbulent 2.5-D flows that evolved based on the Navier–Stokes equations were first performed by Smith & Tobias (2004). They considered flows in the absence of large-scale dissipation. Despite the large Reynolds numbers used, the inverse cascade of energy led to a large-scale condensate that took the form of a vortex dipole which drove the dynamo instability. The flow, despite its almost laminar structure, resulted in fast dynamo action. The behaviour of the growth rate for a wide range of Reynolds numbers (both kinetic and magnetic) was examined. In particular, this flow was the first to demonstrate the persistence of dynamo action in the small magnetic Prandtl number limit (the ratio of viscosity to magnetic diffusivity). The role of these large-scale coherent structures in the dynamo was further studied in Tobias & Cattaneo (2008a,b), where a modified version of the 2-D Navier–Stokes equations (Pierrehumbert, Held & Swanson 1994) that allowed the energy spectrum of the flow to vary was used. A differentiation between the scales ℓ responsible for the dynamo was made by using spectral filters. They argued that the scales responsible for dynamo action are those which have short times scales (i.e. large shear $S_\ell \propto u_\ell/\ell$) provided that the local Reynolds number (i.e. the Reynolds number based on that scale $Re_\ell = u_\ell \ell/\nu$) is sufficiently large.

The present work considers turbulent 2.5-D dynamos in the absence of large-scale condensates. This is achieved by considering the presence of a linear drag force that dissipates large-scale energy. In geophysics the linear drag force, referred to as Ekman friction, models the boundary-layer drag force on large-scale flow dynamics. The amplitude of the drag force is tuned so that the inverse cascade is damped before the largest scales of the system are excited. Thus, no condensates are formed and a continuous turbulent spectrum of excited scales is present. The study is based on numerical simulations of forced 2.5-D turbulence in a 2-D periodic box. Both helical and non-helical flows are considered. The aim of this study is to cover a wide range of parameter space for both types of forcing to give a complete description of the dynamo properties of this system.

The rest of the paper is structured as follows. We describe the system in detail in §2 and discuss the hydrodynamic cascades that happen in this set-up in §3. The results for helical forcing are presented in §4 and the results for non-helical forcing are given in §5. The critical magnetic Reynolds number is discussed in §6. The dependence of the dynamo instability with respect to the forcing length scale is discussed in §7. We present our conclusions in §8.

2. Governing equation

We consider a 2.5-D flow in a periodic box of size $[2\pi L, 2\pi L, H]$ where the height H is along the invariant direction z. The equations governing the velocity field $\boldsymbol{u} = \boldsymbol{u}_{2\text{-}D} + u_z\hat{\boldsymbol{e}}_z = \boldsymbol{\nabla} \times (\psi\hat{\boldsymbol{e}}_z) + u_z\hat{\boldsymbol{e}}_z$ are

$$\left.\begin{aligned}\partial_t \Delta\psi + (\boldsymbol{\nabla} \times \psi\hat{\boldsymbol{e}}_z) \cdot \boldsymbol{\nabla}\Delta\psi &= \nu\Delta^2\psi - \nu_h\Delta\psi + \Delta f_\psi, \\ \partial_t u_z + (\boldsymbol{\nabla} \times \psi\hat{\boldsymbol{e}}_z) \cdot \boldsymbol{\nabla} u_z &= \nu\Delta u_z + f_z.\end{aligned}\right\} \tag{2.1}$$

The first equation corresponds to the vorticity equation of the 2-D components of the flow and the second equation is an advection equation for the vertical velocity component u_z. Δ stands for the 2-D Laplacian, $\nabla \times$ stands for the curl operator. f_ψ, f_z denote the forcing functions that inject energy to the system. Two forcing functions are used: one with mean helicity and the other without any mean helicity. More precisely, we chose $f_\psi = f_z = \cos(k_f x) + \sin(k_f y)$ for the helical case and $f_\psi = \cos(k_f x) + \sin(k_f y)$, $f_z = \sin(k_f x) + \cos(k_f y)$ for the non-helical case. It is noted that for the helical case the helicity of the forcing is given by $-\langle f_z \Delta f_\psi \rangle > 0$ whereas for the non-helical case $-\langle f_z \Delta f_\psi \rangle = 0$. ν is the viscosity and ν_h is the large-scale dissipation coefficient (Ekman friction). The term proportional to ν_h models the effect of the drag force experienced by flow due to boundary-layer effects (Ekman 1905; Pedlosky 1987; Sous, Sommeria & Boyer 2013). We consider only a large-scale dissipation for the evolution of $\boldsymbol{u}_{2\text{-}D}$ because the energy of the u_z component of the flow does not cascade to the large scales. In addition, the absence of a large-scale dissipation in the u_z equation allows a decorrelation of u_z from the vorticity $\omega_z = -\Delta \psi$ that would otherwise follow the same equation (with the same forcing for the helical case).

The evolution of the magnetic field is governed by the induction equation. Due to the invariance of the flow in the z direction, the magnetic field can be decomposed into Fourier modes in z, $\boldsymbol{B} = \boldsymbol{b}(x, y, t) \exp(\mathrm{i}k_z z)$, where $\boldsymbol{b}$ is a three-component complex vector field. Each k_z-mode evolves independently and the induction equation reads

$$\partial_t \boldsymbol{b} + (\nabla \times \psi \hat{\boldsymbol{e}}_z) \cdot \nabla \boldsymbol{b} + u_z \mathrm{i}k_z \boldsymbol{b} = \boldsymbol{b} \cdot \nabla(\nabla \times \psi \hat{\boldsymbol{e}}_z) + \eta(\Delta - k_z^2)\boldsymbol{b}, \qquad (2.2)$$

where η is the magnetic diffusion. The divergence-free condition $\nabla \cdot \boldsymbol{B} = 0$ for each magnetic mode gives

$$\partial_x b_x(x, y, t) + \partial_y b_y(x, y, t) = -\mathrm{i}k_z b_z(x, y, t). \qquad (2.3)$$

There are different ways to non-dimensionalize the system. Here, we are going to use the forcing length scale k_f^{-1} and the root-mean-square value of the total velocity $U = \langle |\boldsymbol{u}_{2\text{-}D}|^2 + u_z^2 \rangle^{1/2}$, where the angular brackets $\langle \cdot \rangle$ denote the spatial and time average. However, we note that U is not controlled in the simulations but is measured *a posteriori*. Alternatively, we can use the forcing amplitude that is controlled in the simulations. However, since the forcing amplitude does not appear in the induction equation where most of the focus of our work lies, we have chosen U. The non-dimensional control parameters of this system are $Re = U/\nu k_f$ the fluid Reynolds number, $Rm = U/\eta k_f$ the magnetic Reynolds number, $k_f L$ the forcing wavenumber and a Reynolds number based on the large-scale friction $R_h = Uk_f/\nu_h$. A fifth non-dimensional number is given by the aspect ratio L/H; however, since each k_z mode evolves independently, we can equivalently consider $k_z L$ as the fifth control parameter.

The equations are solved numerically on a double periodic domain of size $[2\pi L, 2\pi L]$ using a standard pseudo-spectral scheme and a Runge–Kutta fourth-order scheme for time integration (see Gomez, Mininni & Dmitruk 2005). The initial condition for both the magnetic and kinetic field is given by a sum of a few Fourier modes with random phases. Initially a hydrodynamic steady state is obtained by solving only the hydrodynamic equations at a particular Re, $k_f L$. With this steady state, the dynamo simulation is begun with a seed magnetic field and by evolving both the velocity and the magnetic field. The magnetic field starts to grow or decay
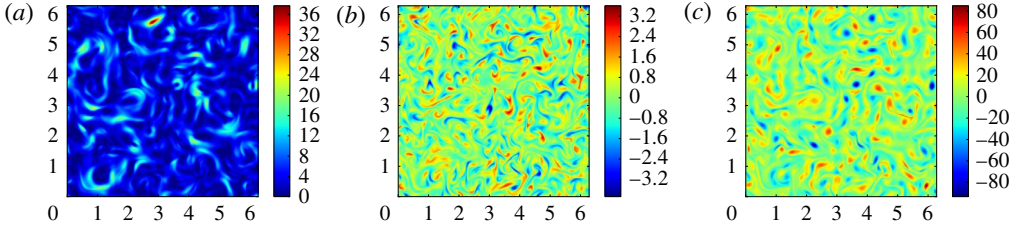
FIGURE 1. (Colour online) The 2-D kinetic energy density $(\partial_x\psi)^2 + (\partial_y\psi)^2$ (*a*), the vertical velocity u_z (*b*) and the vorticity $\Delta\psi$ (*c*) for a non-helical flow with $k_f = 16$.

Case	A1	A2	A3
k_fL	4	8	16
N	[256, 2048]	[512, 2048]	[512, 2048]
Re	[0.5, 1200]	81, 92	91, 97
Rm	[0.1, 2000]	[0.5, 1000]	[0.5, 1000]
R_h	[35, 53]	[163, 184]	[364, 389]
k_zL	[0, 21]	[0, 31]	[0, 45]
T	[300, 2000]	[300, 600]	[300, 600]

TABLE 1. Range of values of each parameter explored in the direct numerical simulations separated into three cases based on the forcing wavenumber k_fL. N is the numerical resolution in each direction and T is the typical eddy turnover time from which the growth rate is calculated.

depending on the control parameters in the system. We define the growth rate of the magnetic field as

$$\gamma = \lim_{t\to\infty} \frac{1}{2t} \log \frac{\langle |\boldsymbol{b}|^2(t)\rangle}{\langle |\boldsymbol{b}|^2(0)\rangle}, \tag{2.4}$$

and γ then depends on all the non-dimensional parameters Re, Rm, k_zL and k_fL. A table of runs is shown in table 1 indicating the range of values of the parameters examined.

3. Hydrodynamic flow and cascades

We first describe the hydrodynamic structure of the flow. A visualization of the 2-D kinetic energy density $(\partial_x\psi)^2 + (\partial_y\psi)^2$, the u_z component of the flow and the vorticity ω_z is shown in figure 1. While the 2-D energy is concentrated at large scales forming large vortices, the vorticity and the vertical velocity are concentrated at small scales showing both vortex and filamentary structures.

The quantities conserved by the nonlinearities in the hydrodynamic equations are the enstrophy in the *x–y* plane $\Omega = \langle\omega_z^2\rangle$ with $\omega_z = -\Delta\psi$, where the angular brackets $\langle\cdot\rangle$ denote spatial average, the energy in the *x–y* plane $E_{2\text{-}D} = \langle\boldsymbol{u}_{2\text{-}D}\cdot\boldsymbol{u}_{2\text{-}D}\rangle/2$, the energy of the z component of velocity $E_z = \langle u_z^2\rangle/2$ and the helicity $H = \langle u_z\omega_z\rangle$. For a more detailed discussion on the invariants, see Smith & Tobias (2004). For a sufficiently small viscosity ν and damping ν_h, the conserved quantities cascade either to small or large scales. For a turbulent 2-D flow there is a forward cascade of enstrophy Ω and an inverse cascade of energy $E_{2\text{-}D}$. E_z has a forward cascade since
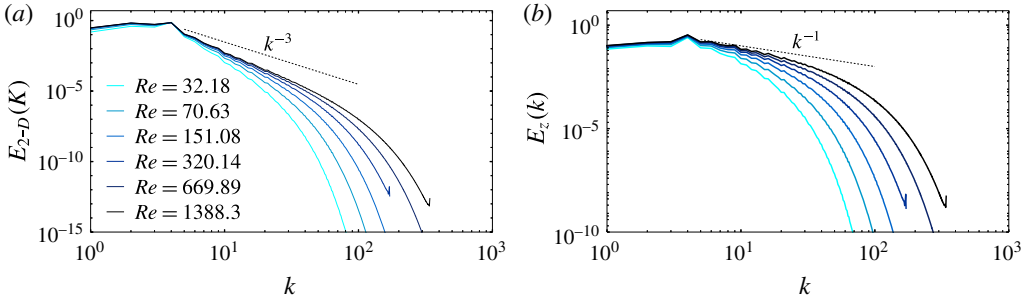
FIGURE 2. (Colour online) The spectra of the 2-D kinetic energy $E_{2\text{-}D}(k)$ and the spectra of the vertical velocity $E_z(k)$ for different values of Re mentioned in the legend. The spectra correspond to non-helical forcing case. The dashed lines show the scaling, k^{-3} in (a) and k^{-1} in (b).

u_z is passively advected and thus has the same phenomenology as passive scalars (Batchelor 1959). Helicity cascades to small scales since both E_z and Ω cascade to small scales. Between the forcing scale and the dissipation scale there exists a range of scales (the inertial range) where the energy spectra have a power-law behaviour $E(k) \propto k^a$ for some exponent a. The exponent a of these power laws is determined by the cascading quantities in the classical Kolmogorov phenomenology. For 2.5-D flows, the exponent of the $E_{2\text{-}D}$ spectrum is -3 in scales smaller than the forcing scale due to the enstrophy cascade and $-5/3$ in scales larger than the forcing scale due to the inverse energy cascade. Similarly, for the spectra of E_z we have -1 in the scales smaller than the forcing scale due to the forward cascade E_z which is similar to the variance of a passive scalar (Batchelor 1959). Since there is no inverse cascade for E_z, we expect equipartition among modes at scales larger than the forcing scale that leads to the exponent $+1$.

Figure 2 shows the spectra $E_{2\text{-}D}$ and E_z for different values of Re for non-helical forcing. The spectra for helical forcing are very similar to the spectra of the flows with non-helical forcing so they are not shown here. The figure shows that the exponents of $E_{2\text{-}D}$ and E_z in the forward cascade change as we increase Re. As shown in Boffetta (2007), the exponent for the energy spectra at small scales tends to be the expected value of -3 as the Re becomes large. In their study, they used numerical grids of up to $32\,768^2$ points to get the expected k^{-3} spectrum. In this work, since the focus is on the dynamo effect, the simulations are done using resolutions only up to 2048^2 grid points, and thus the exponent in the spectra is less than -3. Figure 3 shows the spectra $E_{2\text{-}D}$ and E_z as $k_f L$ is varied for the non-helical forcing. Due to the presence of an inverse cascade, the energy spectra form a $k^{-5/3}$ for scales larger than the forcing scale. For the vertical velocity spectra, the large scales form an equipartition spectrum of k^{+1}. The inverse cascade of energy is dissipated by the friction at large scales which inhibits the formation of a large-scale condensate.

The transfer of kinetic energy to magnetic energy is achieved by the shearing of magnetic lines. Thus, the amplitude of the shear is a determinant quantity for dynamo action that deserves some further discussion. In general, besides the shear amplitude, the dynamo growth rate is also a function of the Reynolds number, the coherence and the complexity of the flow among other quantities (Tobias & Cattaneo 2008a,b; Tobias & Cattaneo 2015). However, for a sufficiently complex and random flow, and if the magnetic Reynolds number is large enough to ignore the dissipative effects from
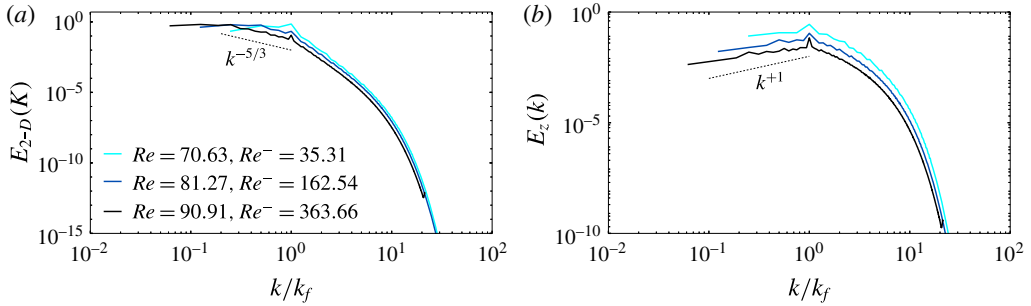
FIGURE 3. (Colour online) The spectra of the 2-D kinetic energy $E_{2\text{-}D}(k)$ and the spectra of the vertical velocity E_z as a function of the rescaled wavenumber k/k_f for different values of Re and $k_f L$ mentioned in the legend. The spectra correspond to the non-helical forcing case. The dashed lines show the scaling, $k^{-5/3}$ in (a) and k^{+1} in (b).

dimensional arguments alone, one expects that the growth rate will be proportional to the largest shear of the flow. This is a speculation that does not take into account some of the particularities of 2.5-D flows. Nonetheless, it is worth considering where the largest shear in the turbulent 2.5-D flows lies.

In 2-D turbulence, the shear $S_{2\text{-}D}^\ell$ in $\boldsymbol{u}_{2\text{-}D}$ at a scale ℓ can be estimated by $S_{2\text{-}D}^\ell \propto u_{2\text{-}D}^\ell/\ell$, where $u_{2\text{-}D}^\ell$ is the amplitude of the $\boldsymbol{u}_{2\text{-}D}$ at a scale ℓ. We know that for 2-D turbulence $u_{2\text{-}D}^\ell \sim \ell$, and hence $S_{2\text{-}D}^\ell$ is the same at all scales between the forcing and the small scale dissipation. Thus, for any $\ell_f > \ell > \ell_v$ we have $S_{2\text{-}D}^\ell \sim S_f = u_f/\ell_f$, where the index f indicates the forcing scale. This is strictly true for k^{-3} spectra, which are seen at very large Re. Since this study uses an exponent that is less than -3 for the most part, at small scales we have $S_{2\text{-}D}^\ell < S_f$. At large scales $u_\ell \propto \ell^{1/3}$ and thus $S_\ell \propto \ell^{-2/3}$. Thus, for any $\ell > \ell_f$ we also have $S_{2\text{-}D}^\ell < S_f$ again. Therefore, the maximum of $S_{2\text{-}D}^\ell$ is found at the forcing scale ℓ_f.

For the vertical velocity field, the shear can be estimated by $S_z^\ell \propto u_z^\ell/\ell$, where u_z^ℓ is the magnitude of u_z at scale ℓ. At small scales, u_z^ℓ follows the scaling $u_z^\ell \propto \ell^0$ and the shear $S_z^\ell \propto \ell^{-1}$ increases as ℓ decreases. Thus, it is maximal at the smallest scales ℓ_v where we obtain $S_z^{\ell_v}\ell_f/u_f \sim Re^{1/2}$. Therefore, $S_{2\text{-}D}^\ell$ is largest at the forcing scale whereas S_z^ℓ is largest at the viscous scales. However, the dynamo instability requires the presence of both S_z and S_ℓ. Thus, we cannot determine which scales are responsible for dynamo action *a priori* or even if such distinction among scales makes sense.

4. Helical dynamos

4.1. *Dependence of γ on k_z*

We first focus on the helical forcing, the laminar case of which corresponds to the case studied by Roberts (1972). Figure 4 shows the growth rate γ as a function of k_z for different values of Rm that are mentioned in the legend and for a fixed $Re \approx 46$. The number of unstable k_z modes increases as we increase Rm as has been observed in other laminar and turbulent studies (Roberts 1972; Smith & Tobias 2004; Tobias & Cattaneo 2008a). As we increase Rm the growth rates for the $k_z \sim O(1)$ modes saturate.

There are unstable dynamo modes for all values of Rm, but the range of unstable modes becomes smaller as Rm is reduced. This can be attributed to the α effect which
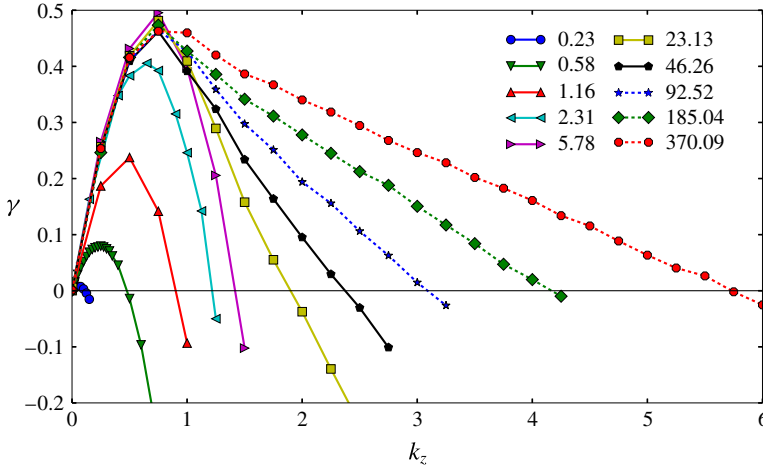
FIGURE 4. (Colour online) The growth rate γ as a function of k_z for the helical forcing case for different values of Rm mentioned in the legend for $Re \approx 46$.

is a mean field effect that can amplify the magnetic field at arbitrarily large scales. In the mean field description, the large-scale magnetic field $\overline{B}$ obeys the equation

$$\partial_t \overline{B} = \nabla \times (\alpha \overline{B}) + \eta_T \Delta \overline{B}, \tag{4.1}$$

where $\boldsymbol{\alpha}$ is in general a tensor and η_T is the turbulent diffusivity. For isotropic flows, the diagonal terms in the $\boldsymbol{\alpha}$ tensor are equal and are responsible for the dynamo effect. They can be calculated numerically by imposing a uniform magnetic field $\boldsymbol{B}_0$ and measuring the induced field $\boldsymbol{b}$ (see Courvoisier *et al.* 2006; Brandenburg Rädler & Schrinner 2008):

$$\boldsymbol{\alpha} \cdot \boldsymbol{B}_0 = \langle \boldsymbol{u} \times \boldsymbol{b} \rangle, \tag{4.2}$$

$$\partial_t \boldsymbol{b} + \boldsymbol{u} \cdot \nabla \boldsymbol{b} = \boldsymbol{b} \cdot \nabla \boldsymbol{u} + \boldsymbol{B}_0 \cdot \nabla \boldsymbol{u} + \eta \Delta \boldsymbol{b}. \tag{4.3}$$

In the small Rm limit, $\eta_T = \eta$ and the α coefficient can be calculated analytically (see Childress 1969; Moffatt 1978; Krause & Raedler 1980; Plunian & Rädler 2002; Gilbert 2003; Brandenburg 2009) leading to the scaling $\alpha \sim uRm$. In either case, the resulting growth rate for the problem at hand is given by

$$\gamma = \alpha k_z - \eta_T k_z^2. \tag{4.4}$$

Figure 5(*a*) shows the γ–k_z curve on a log–log scale with the straight lines indicating the linear scaling αk_z, with α calculated from (4.2) and (4.3). This demonstrates that the behaviour of γ in the small k_z limit is well described by the α effect. Figure 5(*b*) shows the dependence of α as a function of Rm for two different Re. For a turbulent flow and for small Rm, the α coefficient scales as $\alpha \sim uRm$ (see Gilbert 2003), which is captured well by the numerical data. For large Rm, the α value saturates to a constant of the same order as the velocity field. This is different from what has been observed in chaotic flows in Courvoisier *et al.* (2006), where the α coefficient varies rapidly as one increases Rm.

Figure 6 shows the total magnetic energy spectra $E_B(k)$ (where $k = \sqrt{k_x^2 + k_y^2}$) for different values of Rm, a fixed $k_z = 0.25$ and $Re \approx 530$. When the α effect is more pronounced, the magnetic spectra are concentrated at large scales. This occurs in the
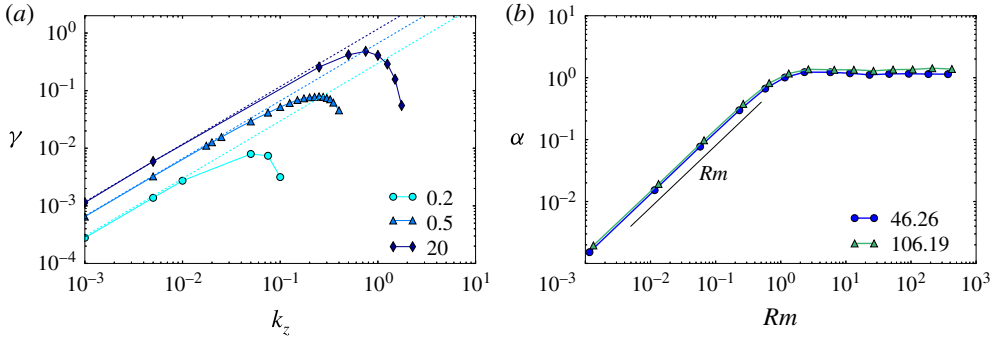
FIGURE 5. (Colour online) (*a*) The growth rate γ as a function of k_z on a log–log scale. The corresponding α values are shown by the dotted straight lines at values of Rm mentioned in the legend. (*b*) α as a function of Rm for the two different Re mentioned in the legend.
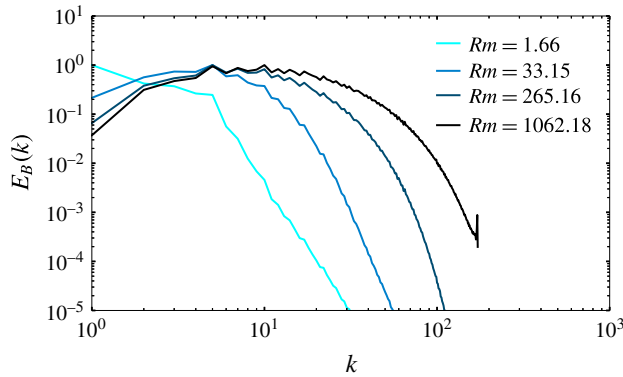

FIGURE 6. (Colour online) The magnetic energy spectra $E_B(k)$ as a function of the wavenumber k for the different Rm shown in the legend. These correspond to a Reynolds number $Re \approx 530$ and to the helical forcing case.

small Rm limit. For large Rm, the magnetic energy spectra become more concentrated towards smaller scales.

4.2. γ_{max} and k_z^c

To quantify the behaviour of γ as we change both Re and Rm, we consider two quantities γ_{max} and k_z^c which characterize the curves shown in figure 4. γ_{max} is the maximum growth rate for given Re and Rm, whereas k_z^c is the largest k_z that is an unstable dynamo for given Re and Rm. Figure 7 shows γ_{max} and k_z^c as functions of Rm for different values of Re. It can be seen that γ_{max} is independent of Re. In the small Rm limit, the behaviour of γ_{max} is governed by the α effect, which gives a scaling $\gamma_{max} \propto Rm^3$ obtained by finding the maximum of (4.4). For large Rm, the γ_{max} approaches a finite asymptote and thus it is a fast dynamo. The most unstable length scale is close to the forcing scale.

In the plot of k_z^c in the small Rm limit, the behaviour is dominated by the α effect leading to $k_z^c \propto Rm^2$ obtained from (4.4). In this limit, k_z^c does not depend on Re
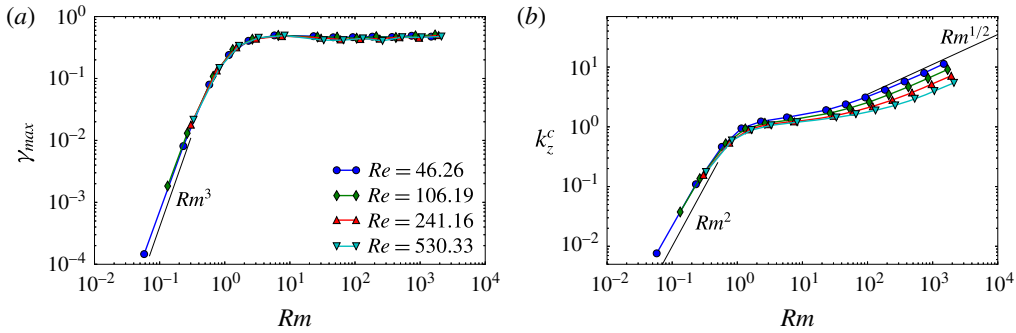
FIGURE 7. (Colour online) γ_{max} (*a*) and k_z^c (*b*) as a function of *Rm* for the different values of *Re* mentioned in the legend for the helical forcing case.
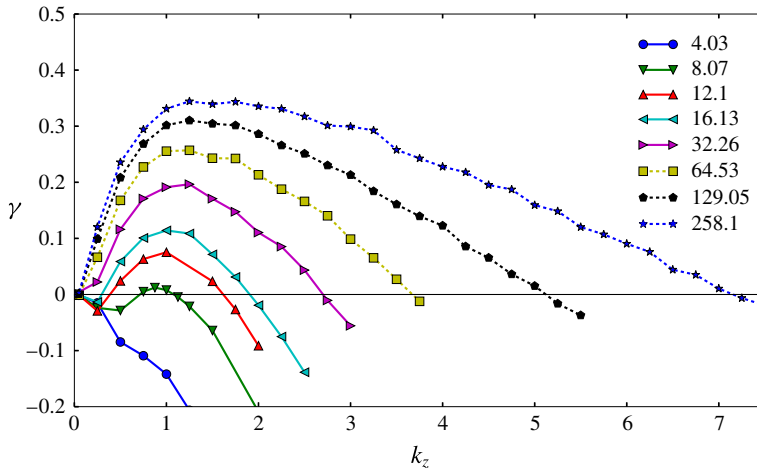

FIGURE 8. (Colour online) The growth rate γ as a function of k_z for the different values of *Rm* mentioned in the legend for $Re \approx 32$. The curves correspond to the non-helical forcing case.

since $k_z^c = cRm^2$ with *c* being independent of *Re*. For large values of *Rm*, we see the scaling $k_z^c \propto Rm^{1/2}$ which can be obtained by balancing the ohmic dissipation with the stretching term. We can also see a clear decrease with the increase of *Re*, which will be discussed in §6.1.

5. Non-helical dynamos

5.1. *Dependence of γ on k_z*

The growth rate γ is shown as a function of k_z for different values of *Rm* in figure 8. Unlike the helical case, there is no dynamo for small *Rm* due to the absence of a mean field α effect. For sufficiently large *Rm*, dynamo instability occurs with the magnetic spectra concentrated at small scales which is similar to the large *Rm* case of the helical forcing shown in figure 6. As *Rm* is increased, the number of unstable modes increases.
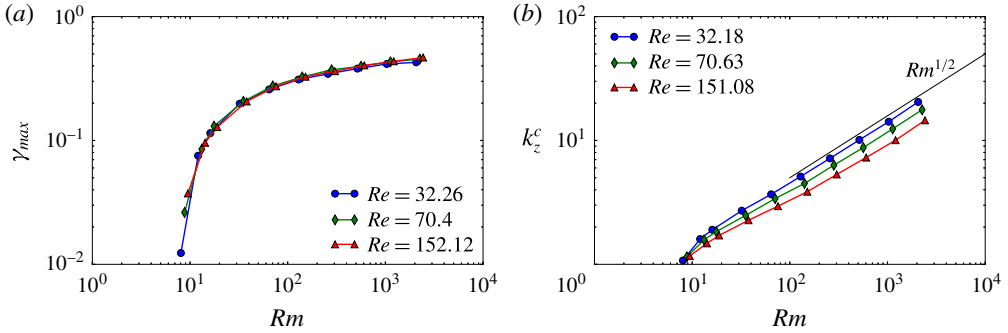
FIGURE 9. (Colour online) γ_{max} (*a*) and k_z^c (*b*) as a function of *Rm* for the different values of *Re* mentioned in the legend. The curves correspond to the non-helical forcing case.
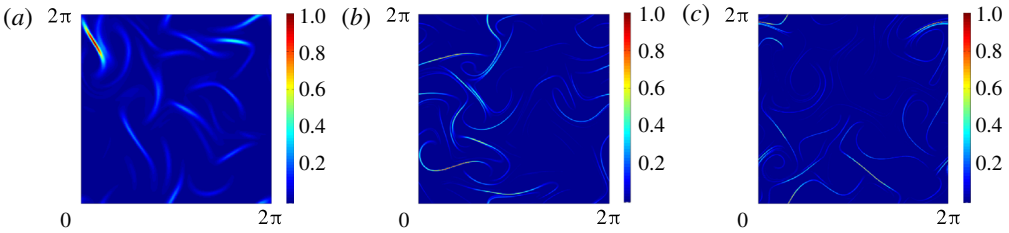

FIGURE 10. (Colour online) Contour of the magnetic energy $B_{2\text{-}D}$ for different values of *Rm*. From (*a*–*c*) we have $Rm \approx 32$, $Rm \approx 1030$ and $Rm \approx 2060$, with $Re \approx 32$ for all three contours. The figures correspond to the non-helical forcing case.

5.2. γ_{max} and k_z^c

Figure 9 shows γ_{max} and k_z^c as a function of *Re* and *Rm*. The dynamo instability starts at $Rm \approx 10$, which is the critical magnetic Reynolds number for this flow. Unlike the helical case, the maximum growth rate γ_{max} increases slowly with *Rm* and a clear asymptote has not yet been reached. *Re* does not seem to affect the behaviour of the γ_{max} curve, indicating that the most unstable modes are not affected by the smallest viscous scales. The scaling of $k_z^c \sim Rm^{1/2}$ in the large *Rm* limit is observed with a prefactor that decreases as *Re* is increased, which is similar to the helical case. The magnetic field generated at small scales is spatially concentrated in thin filamentary structures. Figure 10 shows the contours of magnetic energy in the plane, $|B_{2\text{-}D}|^2 = |b_x|^2 + |b_y|^2$, for increasing values of the magnetic Reynolds number *Rm*. These structures become thinner as we increase *Rm* with the thickness scaling, as $Rm^{-1/2}$. This gives a physical interpretation for the scaling $k_z^c \sim Rm^{1/2}$ seen in figures 7 and 9 in terms of *H*: these filaments should be thinner than the box height *H* for the dynamo instability to take place.

6. Critical magnetic Reynolds number Rm_c

6.1. *Layers of finite thickness*

In general, the onset of dynamo instability depends on the domain size since it determines the available magnetic modes. A flow results in a dynamo if at least one of those modes is unstable. For a given height, *H*, the allowed wavenumbers satisfy
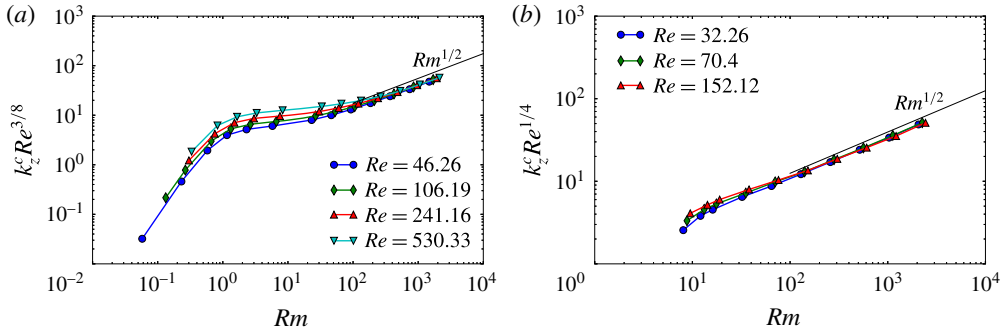
FIGURE 11. (Colour online) $k_z^c Re^\zeta$ as a function of Rm for the different values of Re shown in the legend, for the helical forcing case (*a*) and the non-helical forcing case (*b*).

$k_z \geqslant 2\pi/H \equiv k_z^H$. We thus define a critical magnetic Reynolds number Rm_c based on H as the maximum Rm for which all allowed k_z modes are decaying,

$$Rm_c^H(Re, k_z^H) = \max\{Rm \text{ s.t. } \gamma \leqslant 0 \ \forall k_z > k_z^H\}. \tag{6.1}$$

Thus, for $Rm > Rm_c^H$ there is at least one $k_z > k_z^H$ that is a dynamo. The value Rm_c^H can be calculated from figures 7 and 9 with the condition that the marginal k_z for dynamo equals the minimum allowed wavenumber $k_z^c(Re, Rm) = k_z^H$. For the helical case in the small Rm limit, we get the relation $Rm_c^H \propto \sqrt{k_z^H}$ based on the α effect. Thus, for large H, a small Rm is sufficient for dynamo instability $Rm_c^H \propto (H)^{-1/2}$ with the proportionality coefficient being independent of Re.

The behaviour of Rm_c^H for thin layers ($k_z^H \gg k_f$) depends on Re for both the forcing cases considered. In order to measure this dependence on Re, we rescale k_z^c with Re and replot it as a function of Rm. Figure 11 shows the rescaled cutoff wavenumber $k_z^c Re^\zeta$ for the two different types of forcing studied. Here ζ is an exponent used to collapse the data at large k_z. For the helical forcing we find a best fit of $\zeta = 0.37 \cdots \approx 3/8$ and for the non-helical forcing we find a best fit of $\zeta = 0.25 \cdots \approx 1/4$. This implies that the critical magnetic Reynolds number scales like $Rm_c^H \propto Re^{2\zeta} \sqrt{k_z^H}$. This is unlike the 3-D dynamos (Ponty *et al.* 2005; Iskakov *et al.* 2007; Mininni 2007) for which Rm_c is found to reach a constant value in the large Re limit. However, given that $\zeta < 1/2$, in the limit of large Re, $Rm_c^H \ll Re$ and thus, as with 3-D turbulence, a dynamo can be achieved for any magnetic Prandtl number $Pm = Rm/Re$ provided R_m is large enough. Whether this behaviour persists for very large Re remains to be seen.

6.2. *Infinite layers*

As seen in figure 4, in helical flows, due to the α effect for any Rm, there always exists k_z small enough such that the modes are dynamo unstable. Thus, for a layer that is infinitely thick, a helical flow does not have a critical magnetic Reynolds number since unstable modes exist even for $Rm \to 0$. However, for the non-helical case, there is a critical Rm for the dynamo instability as can be seen in figures 8 and 9. Below this Rm_c, for any mode k_z, there is no dynamo instability. Thus, the critical magnetic Reynolds number Rm_c in the infinite domain is defined as

$$Rm_c(Re) = \max\{Rm \text{ s.t. } \gamma \leqslant 0 \ \forall k_z\} = \lim_{H \to \infty} Rm_c^H. \tag{6.2}$$
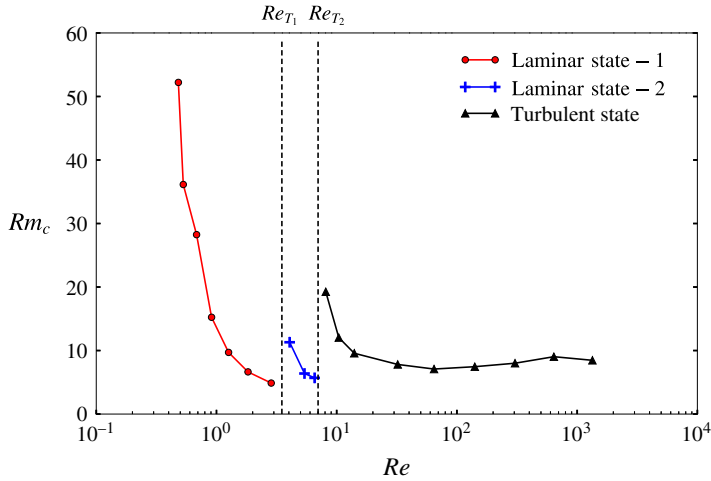
FIGURE 12. (Colour online) The critical magnetic Reynolds number Rm_c as a function of the fluid Reynolds number Re. The two vertical dotted lines denote the two transition Reynolds numbers Re_{T_1}, Re_{T_2}. The curves correspond to the non-helical forcing case.

Note that in practice we do not need an infinitely thick layer to capture the onset of the instability. However, the height H needs to be sufficiently large to allow the first unstable mode $k_z \simeq 1$ (as can be seen in figure 8) to be present. The dependence of Rm_c as a function of Re can be seen in figure 12. Three different regimes corresponding to different flow behaviours are identified and these are separated by vertical dotted lines in the figure denoting the critical Reynolds numbers Re_{T_1} and Re_{T_2}. The curve for $Re > Re_{T_2}$ corresponds to the turbulent regime at large Re and the curves in $Re < Re_{T_1}$, $Re_{T_1} < Re < Re_{T_2}$ correspond to two different laminar flows. Here, Re_{T_2} is the Reynolds number at which the flow transitions between a turbulent state and a laminar state, and Re_{T_1} is the Reynolds number at which the flow transitions between two different laminar time-independent flows. In the limit of large Re we see that the value of Rm_c saturates as is observed in 3-D turbulent flows (Ponty *et al.* 2005; Iskakov *et al.* 2007; Mininni 2007) and the condensate case (Smith & Tobias 2004). Across the transition Reynolds numbers Re_{T_2} and Re_{T_1}, the Rm_c curves have discontinuous behaviour because the flow transitions from one state to the other subcritically. In these laminar states, we find that the growth rate γ scales as k_z^2 for very small k_z as shown in figure 13 for $Re = 0.91 < Re_{T_1}$ in the laminar regime. This scaling indicates that the dynamo action can be explained by the β effect, also known in the literature as the negative magnetic diffusivity effect (see Lanotte *et al.* 1999). The β effect is a mean field effect and the magnetic field is also amplified at the large scales. Figure 14 shows the contour of $|B_{2\text{-}D}|^2 = |b_x|^2 + |b_y|^2$, which is the energy of the magnetic field in the x–y plane. Two different Reynolds number are shown corresponding to the two different laminar states: on the left-hand side $Re_{T_1} < Re = 5.4 < Re_{T_2}$ and on the right-hand side $Re = 0.53 < Re_{T_1}$. Both the plots show large-scale modulations in the magnetic energy at scales close to the box size.

7. Dependence on $k_f L$

In this section, we extend our study to flows with higher values of $k_f L$. The linear damping coefficient is adjusted for each value of $k_f L$ so that the maximum inertial
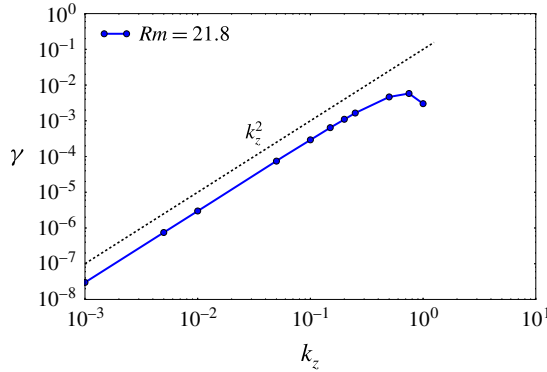
FIGURE 13. (Colour online) The growth rate γ as a function of k_z for a Reynolds number $Re = 0.91 < Re_{T_1}$ together with a dotted line showing the scaling k_z^2. The curve correspond to the non-helical forcing case.
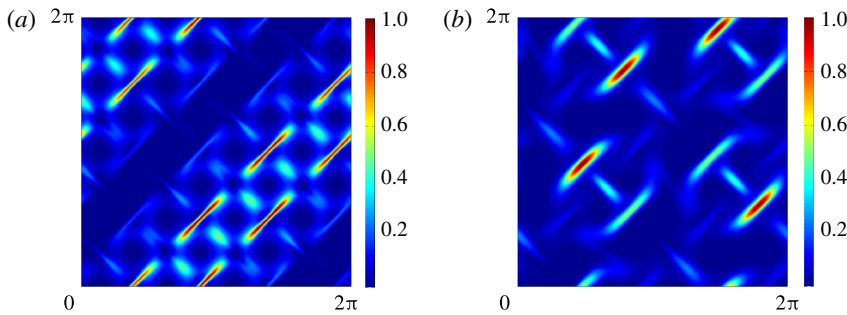

FIGURE 14. (Colour online) Contour of the magnetic energy $B_{2\text{-}D}$ for the two different laminar flows at two different Re – (a) $Re_{T_1} < Re \approx 5.4 < Re_{T_2}$, (b) $Re \approx 0.53 < Re_{T_1}$. The contours correspond to the non-helical forcing case.

range for the inverse cascade is obtained without forming condensates. As we increase $k_f L$, the inverse cascade becomes more important. Depending on the scale separation and the forcing used, the relative amplitude of $u_{2\text{-}D}$ and u_z change as we change $k_f L$. Thus, in order to have a fair comparison between the different dynamos, we normalize the growth rates based on the results of the Ponomarenko dynamo (Ponomarenko 1973) where the growth rate is proportional to the product of the vertical velocity $\boldsymbol{u}_z$ and the planar velocity $\boldsymbol{u}_{2\text{-}D}$ divided by the total root-mean-square value. Thus, we define a velocity scale $U_p = (\langle|\boldsymbol{u}_{2\text{-}D}|^2\rangle^{1/2}\langle u_z^2\rangle^{1/2})/(\langle|\boldsymbol{u}_{2\text{-}D}|\rangle^2 + \langle|u_z|\rangle^2)^{1/2}$ with which we normalize the growth rate. Figure 15 shows the normalized growth rate $\gamma/(U_p k_f)$ as a function of the normalized modes k_z/k_f for both helical and non-helical forcing as we increase $k_f L$ for similar values of Re and Rm. Since k_f is increased, the growth rate γ and the number of unstable k_z modes increase. The normalized curves seem to follow a similar trend for both the forcing cases considered here. At relatively large Rm and as the scale separation is increased, the most unstable wavenumber appears to be close to the forcing wavenumber $k_z^{max} \approx k_f/3$ in both the helical and non-helical forcing cases. This implies that the most unstable modes have a similar length scale with forcing and not with the box size.
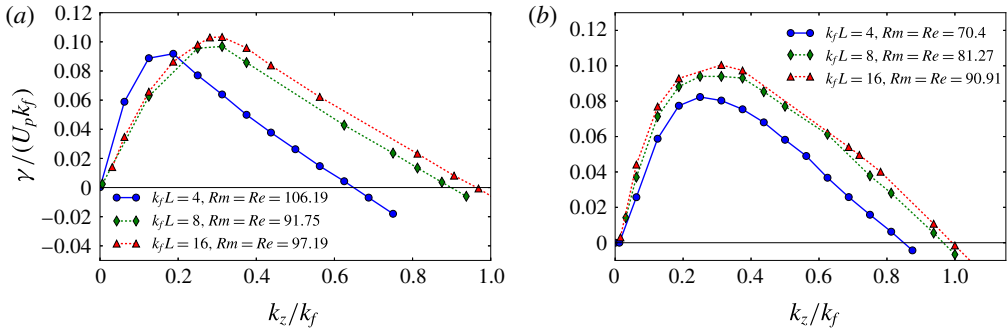
FIGURE 15. (Colour online) $\gamma/(U_p k_f)$ as a function of k_z/k_f for different values of k_f for helical forcing on (*a*) and non-helical forcing on (*b*). The kinetic Reynolds number and the magnetic Reynolds number are mentioned in the legends.

The normalized maximum growth rate $\gamma_{max}/(U_p k_f)$ and the normalized cutoff wavenumber k_z^c/k_f for both helical and non-helical forcing are shown in figure 16. As can be seen from the figures, the normalized quantities follow similar trends to $k_f L = 4$ with weak (or no) dependence on the box size L. Hence, the inverse cascade does not seem to affect the dynamo instability, and the mechanisms of the small-scale dynamo effect and the α dynamo are mostly governed by the forcing scale where the strongest $S_{2\text{-}D}$ shear exists.

8. Conclusions

Our investigation examined the dynamo instability of 2.5-D flows for a wide range of control parameters. This allowed us to test certain limits that are still not attainable in 3-D simulations, and to test asymptotic theories and phenomenological expectations.

For helical flows, we were able to test the alpha dynamo predictions for the behaviour of the large scales ($k_z \ll k_f$) both for small and large values of Rm and Re. The analytical predictions of mean field theories for small values of Rm were verified. For large values of Rm, the growth rates were also shown to be in agreement with a turbulent α dynamo (calculated numerically from (4.2) and (4.3)), and the isotropic α was shown to asymptote to a value independent of Re and Rm. At sufficiently large Rm, the fastest growing mode was always found to have k_z close to the forcing wavenumber. Thus, in a 3-D simulation with random initial conditions for the magnetic field, it is the scales close to the forcing scale that would be observed in the linear stage of the dynamo. This of course does not imply that the large-scale instability does not play a role in the saturated stage of the dynamo and the formation of large-scale magnetic fields at high Rm. To resolve this issue, a nonlinear formalism for the α dynamo would be required.

The non-helical flows were also shown to result in dynamo instability above a value of the magnetic Reynolds number with similar behaviour to the helical dynamo at small scales $k_z \gtrsim k_f$. The critical value of the magnetic Reynolds number for a thin layer of height H was shown to scale similarly to $Rm_c^H \propto Re^{2\zeta}/\sqrt{H}$ with $\zeta \simeq 1/4$ for non-helical flows and $\zeta \simeq 3/8$ for helical flows, implying that there is a dependence of Rm_c^H on Re even at large values of Re. At infinite layer thickness H, the helical flow always resulted in a dynamo (i.e. $Rm_c = 0$). On the other hand, the non-helical flow Rm_c asymptotically reached a finite value in the limit $Re \to \infty$. It is worth pointing
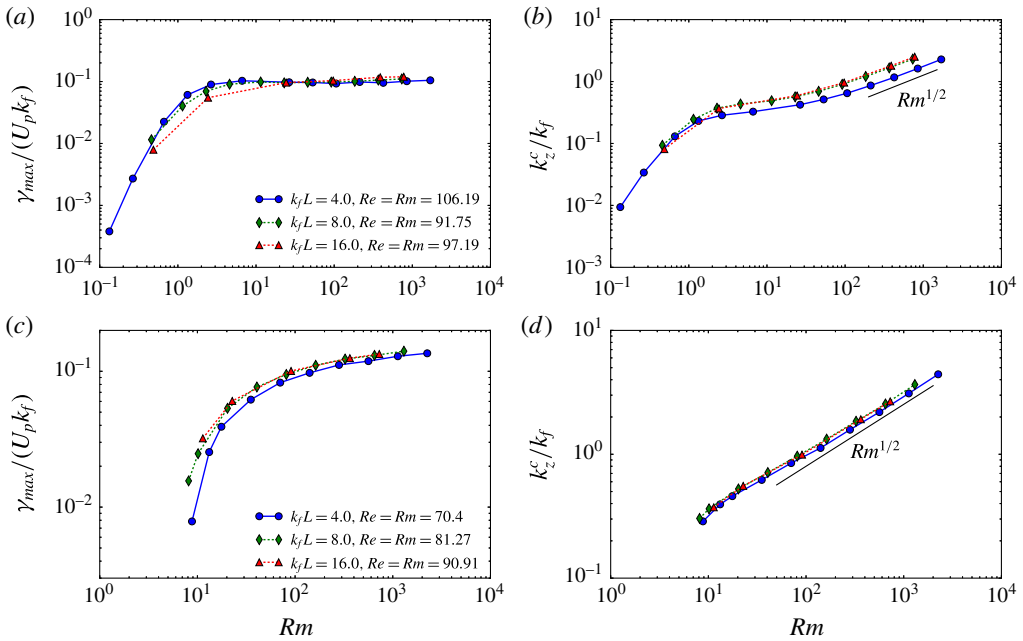
FIGURE 16. (Colour online) Normalized growth rate: $\gamma_{max}/(U_p k_f)$ on (a,c) and k_z^c/k_f on (b,d) for (a,b) helical forcing and (c,d) non-helical forcing as a function of Rm for different $k_f L$ as mentioned in the legends.

out that this asymptotic value $Rm_c \simeq 10$ is almost an order of magnitude smaller than what is obtained in 3-D simulations, and thus rotation could play a beneficial role in liquid-metal experiments.

The investigated dynamo flows were driven by rotating flows that tend to become 2-D at sufficiently large rotation rates. As discussed in the introduction, this is justified for layers of finite thickness and for the periodic boundary conditions above a critical rotation rate that have been considered here. In nature, rotating flows are never fully 2-D, either due to moderate rotation rates or boundary-layer effects.

For moderate rotation rates, large 2-D motions co-exist with 3-D perturbations in the form of travelling inertial waves. The resulting dynamo is then, in general, the result of a combination of these effects. However, due to the fast decorrelation time of inertial waves that has a dynamo suppressing effect (Herreman & Lesaffre 2011), we expect that in rotating flows, even in the presence of some 3-D turbulent fluctuations, the 2.5-D part of the flow would be the dominant effect for a dynamo.

Boundary-layer effects are another way that a flow can deviate from 2-D behaviour in the fast rotating limit. For no-slip boundary conditions, the flow is known to vary rapidly along the rotation direction over a thin layer known as the Ekman layer (Ekman 1905; Pedlosky 1987). This layer is responsible for Ekman friction and the third component of velocity along the direction of rotation due to Ekman pumping. In this case, the amplitude of the third velocity component of the flow (that is essential for dynamo action) depends on the rotation rate. An asymptotic study that investigates these effects for a convection-driven dynamo in the presence of fast rotation was developed in Calkins *et al.* (2015, 2016).

Further investigation of 3-D flows in the presence of rotation are required to address these issues.

Acknowledgements

REFERENCES

ALEXAKIS, A. 2015 Rotating Taylor–Green Flow. *J. Fluid Mech.* **769**, 46–78.

ALEXAKIS, A. & DOERING, C. R. 2006 Energy and enstrophy dissipation in steady state 2d turbulence. *Phys. Lett.* A **359**, 652–657.

BAQUI, Y. B. & DAVIDSON, P. A. 2015 A phenomenological theory of rotating turbulence. *Phys. Fluids* **27** (2), 025107.

BATCHELOR, G. K. 1959 Small-scale variation of convected quantities like temperature in turbulent fluid. Part 1. General discussion and the case of small conductivity. *J. Fluid Mech.* **5** (01), 113–133.

BOFFETTA, G. 2007 Energy and enstrophy fluxes in the double cascade of two-dimensional turbulence. *J. Fluid Mech.* **589**, 253–260.

BOFFETTA, G. & ECKE, R. E. 2012 Two-dimensional turbulence. *Annu. Rev. Fluid Mech.* **44**, 427–451.

VAN BOKHOVEN, L. J. A., CLERCX, H. J. H., VAN HEIJST, G. J. F. & TRIELING, R. R. 2009 Experiments on rapidly rotating turbulent flows. *Phys. Fluids* **21** (9), 096601.

BRANDENBURG, A. 2009 Advances in theory and simulations of large-scale dynamos. *Space Sci. Rev.* **144** (1–4), 87–104.

BRANDENBURG, A., RÄDLER, K.-H. & SCHRINNER, M. 2008 Scale dependence of alpha effect and turbulent diffusivity. *Astron. Astrophys.* **482**, 739–746.

CALKINS, M. A., JULIEN, K., TOBIAS, S. M. & AURNOU, J. M. 2015 A multiscale dynamo model driven by quasi-geostrophic convection. *J. Fluid Mech.* **780**, 143–166.

CALKINS, M. A., JULIEN, K., TOBIAS, S. M., AURNOU, J. M. & MARTI, P. 2016 Convection-driven kinematic dynamos at low Rossby and magnetic Prandtl numbers: single mode solutions. *Phys. Rev.* E **93**, 023115.

CAMPAGNE, A., GALLET, B., MOISY, F. & CORTET, P.-P. 2014 Direct and inverse energy cascades in a forced rotating turbulence experiment. *Phys. Fluids* **26** (12), 125112.

CATTANEO, F. & TOBIAS, S. M. 2014 On large-scale dynamo action at high magnetic Reynolds number. *Astrophys. J.* **789**, 70.

CHEN, Q., CHEN, S., EYINK, G. L. & HOLM, D. D. 2005 Resonant interactions in rotating homogeneous three-dimensional turbulence. *J. Fluid Mech.* **542**, 139–164.

CHERTKOV, M., CONNAUGHTON, C., KOLOKOLOV, I. & LEBEDEV, V. 2007 Dynamics of energy condensation in two-dimensional turbulence. *Phys. Rev. Lett.* **99** (8), 084501.

CHILDRESS, S. 1969 A class of solutions of the magnetohydrodynamic dynamo problem. In *The Application of Modern Physics to the Earth and Planetary Interiors*, pp. 629–648. Wiley.

CONSTANTIN, P., FOIAS, C. & MANLEY, O. P. 1994 Effects of the forcing function spectrum on the energy spectrum in 2-D turbulence. *Phys. Fluids* **6**, 427–429.

COURVOISIER, A., HUGHES, D. W. & TOBIAS, S. M. 2006 α effect in a family of chaotic flows. *Phys. Rev. Lett.* **96** (3), 034503.

DAVIDSON, P. A. 2014 The dynamics and scaling laws of planetary dynamos driven by inertial waves. *Geophys. J. Intl* **198** (3), 1832–1847.

DEUSEBIO, E., BOFFETTA, G., LINDBORG, E. & MUSACCHIO, S. 2014 Dimensional transition in rotating turbulence. *Phys. Rev.* E **90** (2), 023005.

EKMAN, V. W. 1905 On the influence of the earth\'s rotation on ocean currents. *Ark. Mat. Astron. Fys.* **2**, 1–53.

EYINK, G. L. 1996 Exact results on stationary turbulence in 2D: consequences of vorticity conservation. *Physica* D **91**, 97–142.

GALLET, B. 2015 Exact two-dimensionalization of rapidly rotating large-Reynolds-number flows. *J. Fluid Mech.* **783**, 412–447.

GALLET, B., CAMPAGNE, A., CORTET, P.-P. & MOISY, F. 2014 Scale-dependent cyclone-anticyclone asymmetry in a forced rotating turbulence experiment. *Phys. Fluids* **26** (3), 035108.

GALLOWAY, D. J. & PROCTOR, M. R. E. 1992 Numerical calculations of fast dynamos in smooth velocity fields with realistic diffusion. *Nature* **356**, 691–693.

GILBERT, A. D. 2003 Dynamo theory. In *Handbook of Mathematical Fluid Dynamics*, vol. 2, pp. 355–441. Elsevier.

GOMEZ, D. O., MININNI, P. D. & DMITRUK, P. 2005 Parallel simulations in turbulent mhd. *Phys. Scr.* **T116**, 123.

HERREMAN, W. & LESAFFRE, P. 2011 Stokes drift dynamos. *J. Fluid Mech.* **679**, 32–57.

HOPFINGER, E. J. & VAN HEIJST, G. J. F. 1993 Vortices in rotating fluids. *Annu. Rev. Fluid Mech.* **25**, 241–289.

HOSSAIN, M. 1994 Reduction in the dimensionality of turbulence due to a strong rotation. *Phys. Fluids* **6**, 1077–1080.

HOUGH, S. S. 1897 On the application of harmonic analysis to the dynamical theory of the tides. Part I. On Laplace's 'oscillations of the first species, and on the dynamics of ocean currents. *Phil. Trans. R. Soc. Lond.* A **189**, 201–257.

ISKAKOV, A. B., SCHEKOCHIHIN, A. A., COWLEY, S. C., MCWILLIAMS, J. C. & PROCTOR, M. R. E. 2007 Numerical demonstration of fluctuation dynamo at low magnetic prandtl numbers. *Phys. Rev. Lett.* **98** (20), 208501.

IZAKOV, M. N. 2013 Large-scale quasi-two-dimensional turbulence and a inverse spectral flux of energy in the atmosphere of Venus. *Solar Syst. Res.* **47**, 170–181.

KRAICHNAN, R. H. 1967 Inertial ranges in two-dimensional turbulence. *Tech. Rep.* DTIC Document.

KRAUSE, F. & RAEDLER, K.-H. 1980 *Mean-field Magnetohydrodynamics and Dynamo Theory*. Pergamon.

LANOTTE, A., NOULLEZ, A., VERGASSOLA, M. & WIRTH, A. 1999 Large-scale dynamo produced by negative magnetic eddy diffusivities. *Geophys. Astrophys. Fluid Dyn.* **91** (1–2), 131–146.

LAURIE, J., BOFFETTA, G., FALKOVICH, G., KOLOKOLOV, I. & LEBEDEV, V. 2014 Universal profile of the vortex condensate in two-dimensional turbulence. *Phys. Rev. Lett.* **113**, 254503.

MININNI, P. D. 2007 Inverse cascades and α effect at a low magnetic Prandtl number. *Phys. Rev.* E **76** (2), 026316.

MININNI, P. D. & POUQUET, A. 2010 Rotating helical turbulence. I. Global evolution and spectral behavior. *Phys. Fluids* **22** (3), 035105.

MOFFATT, H. K. 1978 *Magnetic Field Generation in Electrically Conducting Fluids*. Cambridge University Press.

NAZARENKO, S. V. & SCHEKOCHIHIN, A. A. 2011 Critical balance in magnetohydrodynamic, rotating and stratified turbulence: towards a universal scaling conjecture. *J. Fluid Mech.* **677**, 134–153.

OTANI, N. F. 1993 A fast kinematic dynamo in two-dimensional time-dependent flows. *J. Fluid Mech.* **253**, 327–340.

PARKER, E. N. 1955 Hydromagnetic dynamo models. *Astrophys. J.* **122**, 293.

PEDLOSKY, J. 1987 *Geophysical Fluid Dynamics*. Springer.

PIERREHUMBERT, R. T, HELD, I. M & SWANSON, K. L 1994 Spectra of local and nonlocal two-dimensional turbulence. *Chaos, Solitons Fractals* **4** (6), 1111–1116.

PLUNIAN, F. & RÄDLER, K.-H. 2002 Subharmonic dynamo action in the Roberts Flow. *Geophys. Astrophys. Fluid Dyn.* **96**, 115–133.

PONOMARENKO, YU. B. 1973 On the theory of the hydrodynamic dynamo. *J. Appl. Mech. Tech. Phys.* **14**, 775–779.

PONTY, Y., MININNI, P. D., MONTGOMERY, D. C., PINTON, J.-F., POLITANO, H. & POUQUET, A. 2005 Numerical study of dynamo action at low magnetic Prandtl numbers. *Phys. Rev. Lett.* **94** (16), 164502.

PROCTOR, M. R. E. & GILBERT, A. D. 1995 *Lectures on Solar and Planetary Dynamos*. Cambridge University Press.

PROUDMAN, J. 1916 On the motion of solids in a liquid possessing vorticity. *Phil. Trans. R. Soc. Lond.* A **92**, 408–424.

RÄDLER, K.-H. & BRANDENBURG, A. 2009 Mean-field effects in the galloway–proctor flow. *Mon. Not. R. Astron. Soc.* **393** (1), 113–125.

ROBERTS, G. O. 1972 Dynamo action of fluid motions with two-dimensional periodicity. *Phil. Trans. R. Soc. Lond.* A **271** (1216), 411–454.

SCOTT, J. F. 2014 Wave turbulence in a rotating channel. *J. Fluid Mech.* **741**, 316–349.

SEN, A., MININNI, P. D., ROSENBERG, D. & POUQUET, A. 2012 Anisotropy and nonuniversality in scaling laws of the large-scale energy spectrum in rotating turbulence. *Phys. Rev.* E **86** (3), 036319.

SMITH, L. M. & WALEFFE, F. 1999 Transfer of energy to two-dimensional large scales in forced, rotating three-dimensional turbulence. *Phys. Fluids* **11**, 1608–1622.

SMITH, S. G. L. & TOBIAS, S. M. 2004 Vortex dynamos. *J. Fluid Mech.* **498**, 1–21.

SOUS, D., SOMMERIA, J. & BOYER, D. L. 2013 Friction law and turbulent properties in a laboratory Ekman boundary layer. *Phys. Fluids* **25** (4), 046602.

STAPLEHURST, P. J., DAVIDSON, P. A. & DALZIEL, S. B. 2008 Structure formation in homogeneous freely decaying rotating turbulence. *J. Fluid Mech.* **598**, 81–105.

SUGIHARA, Y., MIGITA, M. & HONJI, H. 2005 Orderly flow structures in grid-generated turbulence with background rotation. *Fluid Dyn. Res.* **36**, 23–34.

TAYLOR, G. I. 1917 Motion of solids in fluids when the flow is not irrotational. *Proc. R. Soc. London* A **93**, 99–113.

THIELE, M. & MÜLLER, W.-C. 2009 Structure and decay of rotating homogeneous turbulence. *J. Fluid Mech.* **637**, 425.

TOBIAS, S. M. & CATTANEO, F. 2008*a* Dynamo action in complex flows: the quick and the fast. *J. Fluid Mech.* **601**, 101–122.

TOBIAS, S. M. & CATTANEO, F. 2008*b* Limited role of spectra in dynamo theory: coherent versus random dynamos. *Phys. Rev. Lett.* **101**, 125003.

TOBIAS, S. M. & CATTANEO, F. 2013 Shear-driven dynamo waves at high magnetic Reynolds number. *Nature* **497** (7450), 463–465.

TOBIAS, S. M. & CATTANEO, F. 2015 The electromotive force in multi-scale flows at high magnetic Reynolds number. *J. Plasma Phys.* **81** (6), 395810601.

VISHIK, M. M. 1989 Magnetic field generation by the motion of a highly conducting fluid. *Geophys. Astrophys. Fluid Dynam.* **48**, 151–167.

WALEFFE, F. 1993 Inertial transfers in the helical decomposition. *Phys. Fluids* **5**, 677–685.

YAROM, E., VARDI, Y. & SHARON, E. 2013 Experimental quantification of inverse energy cascade in deep rotating turbulence. *Phys. Fluids* **25** (8), 085105.

YEUNG, P. K. & ZHOU, Y. 1998 Numerical study of rotating turbulence with external forcing. *Phys. Fluids* **10**, 2895–2909.

YOSHIMATSU, K., MIDORIKAWA, M. & KANEDA, Y. 2011 Columnar eddy formation in freely decaying homogeneous rotating turbulence. *J. Fluid Mech.* **677**, 154–178.

ZEL'DOVICH, YA. B. 1958 Electromagnetic interaction with parity violation. *Sov. Phys. JETP* **6**, 1184; (*Zh. Eksp. Teor. Fiz.* **33**, 1531 (1957)).